Numerical simulation of 3D bubbles rising in viscous liquids using a front tracking method

Jinsong Hua [a,*], Jan F. Stene [b], Ping Lin [b]

[a] *Institute of High Performance Computing, 1 Science Park Road, #01-01 The Capricorn, Singapore 117528, Singapore*
[b] *Department of Mathematics, National University of Singapore, 2 Science Drive 2, Singapore 117543, Singapore*

Abstract

The rise of bubbles in viscous liquids is not only a very common process in many industrial applications, but also an important fundamental problem in fluid physics. An improved numerical algorithm based on the front tracking method, originally proposed by Tryggvason and his co-workers, has been validated against experiments over a wide range of inter-mediate Reynolds and Bond numbers using an axisymmetric model [J. Hua, J. Lou, Numerical simulation of bubble rising in viscous liquid, J. Comput. Phys. 22 (2007) 769–795]. In the current paper, this numerical algorithm is further extended to simulate 3D bubbles rising in viscous liquids with high Reynolds and Bond numbers and with large density and viscosity ratios representative of the common air–water two-phase flow system. To facilitate the 3D front tracking simulation, mesh adaptation is implemented for both the front mesh on the bubble surface and the background mesh. On the latter mesh, the governing Navier–Stokes equations for incompressible, Newtonian flow are solved in a moving reference frame attached to the rising bubble. Specifically, the equations are solved using a finite volume scheme based on the Semi-Implicit Method for Pressure-Linked Equations (SIMPLE) algorithm, and it appears to be robust even for high Reynolds numbers and high density and viscosity ratios. The 3D bubble surface is tracked explicitly using an adaptive, unstructured triangular mesh. The numerical model is integrated with the software package PARAMESH, a block-based adaptive mesh refinement (AMR) tool developed for parallel computing. PARAMESH allows background mesh adaptation as well as the solution of the governing equations in parallel on a supercomputer. Further, Peskin distribution function is applied to interpolate the variable values between the front and the background meshes. Detailed sensitivity analysis about the numerical mod-eling algorithm has been performed. The current model has also been applied to simulate a number of cases of 3D gas bubbles rising in viscous liquids, e.g. air bubbles rising in water. Simulation results are compared with experimental obser-vations both in aspect of terminal bubble shapes and terminal bubble velocities. In addition, we applied this model to sim-ulate the interaction between two bubbles rising in a liquid, which illustrated the model's capability in predicting the interaction dynamics of rising bubbles.
© 2007 Elsevier Inc. All rights reserved.

---

* Corresponding author. Tel.: +65 6419 1537; fax: +65 6778 0522.
E-mail address: huajs@ihpc.a-star.edu.sg (J. Hua).

1. Introduction

Multiphase flows are numerous in both everyday life and engineering practice [34]. Typical examples in nature include raindrops in air and gas bubbles in water, whereas chemical reactions, combustion and petroleum refining are examples of multiphase flows in industry. One very basic example of such flows is the rise of a single gas bubble in an otherwise quiescent viscous liquid due to buoyancy. The understanding of the flow dynamics of this system is of great importance in engineering applications and to the fundamental understanding of multiphase flow physics. Rising bubbles have been studied theoretically [8,25], experimentally [1] as well as computationally through numerical modeling [37,22]. While all these efforts have provided us with valuable insights into the dynamics of bubbles rising in viscous liquids, there are still many questions that remain unanswered due to the involvement of complex physics. The behavior of a bubble rising in a viscous liquid is not only affected by physical properties such as the density and the viscosity of both phases [6], but also by the surface tension on the interface between the two phases and by the bubble shape evolution [27,2]. The difficulties in describing and modeling the complex behavior of a rising bubble are to a large extent due to the strong nonlinear coupling of factors such as buoyancy, surface tension, bubble/liquid momentum inertia, viscosity, bubble shape evolution and rise history of the bubble. In addition, the physical behavior of bubbles is of three-dimensional in nature. Hence, most of the past theoretical works were done with a lot of assumptions, and the results are only valid for certain flow regimes [25,45]. The experimental works were limited by the available technologies to monitor, probe and sense the moving bubbles without interfering with their physics [1,40,46].

With the rapid advance of computing power and the development of robust numerical methods, direct numerical simulations promise great potential in extending our knowledge of the fundamental system of a single bubble rising in a viscous liquid. However, there are still great challenges and difficulties in simulating such a system accurately. This may be attributed to the following facts: (i) the sharp interface between the gas bubble and the surrounding liquid should be tracked accurately without introducing excessive numerical smearing; (ii) the surface tension gives rise to a singular source term in the governing equations, leading to a sharp pressure jump across the interface; (iii) the discontinuity of the density and viscosity across the fluid interface may lead to numerical instability, especially when the jumps in these properties are high. For example, the density ratio of liquid to gas could be as high as 1000; (iv) the geometric complexity caused by bubble deformation and possible topological change is the main difficulty in handling the geometry of interface; a large bubble may breakup into several small ones, and small bubbles may also merge to form larger bubbles; (v) the complex physics on the interface, e.g. the effects of surfactants, thin liquid film dynamics, film boiling and phase change (heat and mass transfer) and chemical reactions. Fortunately, various methods for multiphase flow have been developed to address these difficulties, and each method typically has its own characteristic strengths and weaknesses. Comprehensive reviews of numerical methods for multiphase/interfacial flow simulation have been given by Scardovelli and Zaleski [39] and van Sint Annaland et al. [43]. Most of the current numerical techniques applied in the simulation of multiphase/interfacial flows have been developed with focus on the following two aspects: (i) capturing/tracking the sharp interface, e.g. interface capturing, grid fitting, front tracking or hybrid methods; and (ii) stabilizing the flow solver to handle discontinuous fluid properties and highly singular interfacial source terms, e.g. the projection–correction method [43] and the SIMPLE algorithm [6,17].

The volume of fluid [14,4], level-set [28,44,29] and phase-field [19] approaches fall into the first category of front capturing methods. In these methods the interface is captured using various volume functions defined on the grid used to solve the "one-fluid" formulation of the governing equations for multiphase flow. Since the interface can be captured using the same grid as the flow solver, these methods are relatively easy to implement. However, the accuracy of this approach is limited by the numerical diffusion from the solution of the convection equation of the volume function. Various schemes have been developed to advect, reconstruct/reinitialize the volume function to improve the accuracy in calculating the interface position. One example is the high-order shock-capturing scheme used to treat the convective terms in the governing equations [18]. Although the explicit reconstruction of the interface is circumvented, the implementation of such high-order schemes is quite complicated, and they do not work well for the sharp discontinuities encountered in multiphase/interfacial flows. In addition, a relatively fine grid is needed in the vicinity of the interface to obtain good resolution.

The second category of these methods tries to track the moving interface by fitting the background grid points according to the interface position. The fitting is achieved through re-meshing techniques such as deforming, moving, and adapting the background grid points. This method is also well known as a "bound-ary-fitting approach", and the "boundary" here refers to the interface between the fluids. The grid-fitting approach [37,20,3] is capable of capturing the interface position accurately. Early development on this approach was done by Ryskin and Leal [37], and curvilinear grids were used to follow the motion of a rising bubble in liquid. This method is suitable for relatively simple geometries undergoing small deformations, whereas applications to complex, fully three-dimensional problems with unsteady deforming phase boundaries are very rare. This is mainly due to difficulties in maintaining the proper volume mesh quality and in handling complex interface geometry such as topological change. In spite of these difficulties, recent works by Hu et al. [16] showed some very impressive results on 3D simulations of moving spherical particles in liquid. Quan and Schmidt [35] presented a meshing adaptation method to track the 3D moving interface in two-phase flows.

The third category is the front tracking method. This approach solves the flow field on a fixed grid and tracks the interface position in a Lagrangian manner by a set of interface markers. These interface markers can be free particles without connection, or they can be logically connected elements, possibly containing accu-rate geometric information about the interface such as area, volume, curvature, deformation, etc. A front tracking technique was proposed by pioneer researchers Glimm and his co-workers [11–13]. They represent the front interface using a set of moving markers and solve the flow field on a separate background grid. The background grid is modified only near the front to make background grid points coincide with the front markers of the interface. In this case, some irregular grids are reconstructed and special finite difference stencils are created for the flow solver, increasing the complexity of the method and making it more difficult to imple-ment. Independently, another front tracking technique was developed by Peskin and collaborators [31,10,32]. In their method, the interface is represented by a connected set of particles that carry forces, either imposed externally or adjusted to achieve a specific velocity at the interface. A fixed background grid is kept unchanged even near the front interface, and the interface forces are distributed onto the background to solve the "one-fluid" formulation of the flow equations.

A number of combinations and improvements of these basic approaches have been proposed to enhance the capabilities in dealing with the sharp, moving interface, where complex physical phenomena and processes could occur. One of the most promising approaches is arguably the front tracking method proposed by Try-ggvason and his collaborators [22,48,47]. Actually, this method may be viewed as a hybrid of the front cap-turing and the front tracking techniques: a fixed background grid is used to solve the fluid flow, while a separate interface mesh is used to track the interface position explicitly. The tracked interface carries informa-tion about jumps in the density and the viscosity and also about interfacial forces such as surface tension. Fluid properties are then distributed onto the fixed background grid according to the position of the interface. The surface tension can be calculated according to the geometry of the interface and is also distributed onto the background grid in the vicinity of the interface.

Besides the numerical techniques employed to capture/track the moving interface, it is also very important to develop a stable numerical method to solve the governing equations of the flow field. Some investigators have considered simplified models such as Stokes flow [33], where inertia is completely ignored, and inviscid potential flow [15], where viscous effects are ignored. In both cases, the motion of deformable boundaries can be simulated with boundary integral techniques. However, when considering the transient Navier–Stokes equations for incompressible, Newtonian fluid flow, the so-called "one-fluid" formulation for multiphase flow has proved most successful [4,44,47]. Popular modern methods that use the "one-fluid" formulation include the projection–correction method [46,43] and the SIMPLE algorithm [6,17]. Various multiphase/interfacial flow problems have been successfully simulated by the front tracking method [47] with a projection–correction flow solver. It appears that previously reported results have been limited to flow with low to intermediate Rey-nolds numbers (<100) and small density ratios (<100) [5]. It is thus natural to re-examine the approach and to make it more robust and applicable to wider flow regimes. Some revised versions of the projection–correction method have been proposed to improve its capability in handling situations with large density and viscosity ratios [43]. Recently, Hua and Lou [17] tested a SIMPLE-based algorithm to solve the incompressible Navier–Stokes equations. The simulation results indicate that the newly proposed method can robustly solve the Navier–Stokes equations with large density ratios up to 1000 and large viscosity ratios up to 500.

Hua and Lou [17] presented extensive simulations and model validation on a single bubble rising in a quiescent liquid. The comprehensive simulations show good results in a wide flow regime with high density and viscosity ratios, and the algorithm is as such promising in the direct numerical simulation of multiphase flow. Unfortunately, the previous validation studies were limited to the 2D axisymmetric model where fluid flows and bubble shapes are axisymmetric. Hence, it would be interesting to investigate the robustness of the proposed numerical approach for multiphase flow in flow regimes of higher Reynolds and Bond numbers where the bubble may not be axisymmetric anymore. Therefore, a fully three-dimensional modeling approach is proposed in this paper. In addition, other features such as mesh adaptation, a moving reference frame and parallel processing are introduced to enhance the model capability in simulating the rise of a 3D bubble in a viscous liquid.

The numerical algorithm proposed by Tryggvason and co-workers [48,47] and extended further by Hua and Lou [17], is adopted in this paper. The handling of the moving interface in this method may be characterized as a hybrid of interface tracking and capturing. The governing Navier–Stokes equations are solved on a fixed Cartesian grid with an adaptive block structure, while the interface is represented by a set of explicitly tracked front markers. These markers form an adaptive triangular surface mesh that is advected with a velocity interpolated from the surrounding fluid. An illustration of such a mesh system is shown in Fig. 1. A single set of the governing equations is solved in the entire computational domain by treating the two fluids as one single fluid with variable fluid properties across the interface – often referred to as the "one-field" or "one-fluid" approach. The interface is assumed to have a given finite thickness (normally about two to four times the background grid size) so that jumps in the fluid properties across the surface can be reconstructed smoothly by solving a Poisson equation.

A parallel adaptive mesh refinement (AMR) tool, PARAMESH [24], is integrated with the modified SIMPLE flow solver, and the governing equations are solved in a non-inertial moving reference frame attached to the rising bubble. The AMR feature allows a relatively high-resolution mesh in the vicinity of the bubble surface. The non-inertial moving reference frame technique translates the computational domain with the rising bubble, allowing the computational domain to be relatively small and always centred around the bubble. The latter feature is particularly useful for studying the path instability of a rising bubble or the interaction of multiple bubbles, which may need very long simulation periods. For example, it is observed in experiments that the paths of millimeter-sized air bubbles rising in water normally stabilize after a rise distance of 50–100 times
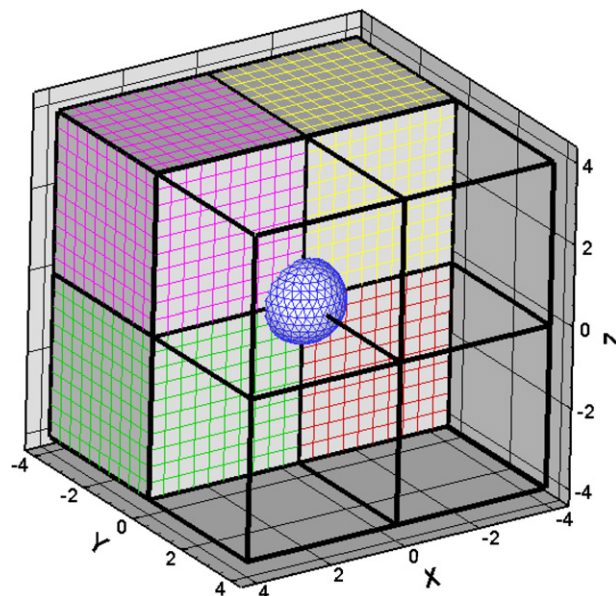

Fig. 1. Simulation of a single bubble rising using the front tracking method. Multiple unstructured blocks with Cartesian mesh are used for the flow solver while the bubble surface is represented by an unstructured triangular mesh.

the initial bubble diameter. If a stationary frame were applied to simulate this situation, the computational domain would be huge compared to the domain of interest. Even though an AMR feature is adopted, the total number of grid points could still be a big burden, slowing down the simulation.

The problem of a single bubble rising in a viscous liquid has been widely used as a typical validation case for the development of new numerical methods for multiphase flow [6,42,43]. Due to numerous experimental and numerical studies in the past, the physical understanding of the bubble rise behavior in liquid has been well established in some flow regimes, e.g. regimes with low Reynolds and Bond numbers [7,1]. However, due to the complexity in multiphase flow physics and the difficulties in both experiments and simulations, the behavior of a rising bubble with high Reynolds number is still not understood well [26,21]. In this paper, we first validate our model through comparing computational results of a single bubble rising with experimental results [1] in aspects of both bubble shapes and terminal velocities. In addition, we apply the 3D model to simulate air bubbles rising in water, and we compare the terminal velocities and shapes of the bubbles predicted in our simulations with experimental results within a large range of bubble diameters: from 0.5 to 30 mm. There have been few numerical studies on this topic except some recent ones [9,21]. However, since the process of air bubbles rising in water is so common in both our daily life and industrial applications, a better understanding of this system is of great importance.

The rest of this paper is organized as follows. In Section 2, we present the governing equations as well as the numerical method to solve these equations. Numerical results presented in Section 3 include a detailed sensitivity analysis of the computational model set-up as well as validation through a comparison of our numerical predictions with available experimental data on gas bubbles rising in liquids. In addition, we also apply the current model to simulate the interaction of two rising bubbles. Finally, we recapitulate our main findings in Section 4.

2. Mathematical model and numerical method

2.1. Governing equations

The problem of gas bubbles rising in liquids studied in this paper can be described as an isothermal, multi-fluid system with two incompressible and immiscible Newtonian fluids. We will use one single set of governing equations for the entire flow domain where we treat the different fluids as one single fluid with material properties varying across the interface. With this "one-fluid" approach, there is no need to deal with the jump conditions across the interface when the governing equations are solved. However, we will have to calculate the fluid property distributions and include the surface tension as a singular source term in the solution domain through the use of a delta function before the equations can be solved.

The mass conservation for the whole domain under the incompressibility condition may be expressed as

$$\nabla \cdot \mathbf{u} = 0. \tag{1}$$

The momentum conservation (Navier–Stokes equations) takes the form

$$\frac{\partial(\rho \mathbf{u})}{\partial t} + \nabla \cdot \rho \mathbf{u}\mathbf{u} = -\nabla p + \nabla \cdot [\mu(\nabla \mathbf{u} + \nabla^{\mathrm{T}}\mathbf{u})] + \int_{\Gamma} \sigma_{\mathrm{f}} \kappa_{\mathrm{f}} \mathbf{n}_{\mathrm{f}} \delta(\mathbf{x} - \mathbf{x}_{\mathrm{f}}) \mathrm{d}s + (\rho - \rho_{\mathrm{l}})\mathbf{g}, \tag{2}$$

where $\mathbf{u}$ is the fluid velocity, ρ is the fluid density, ρ_{l} is the density of the liquid phase, p is the pressure, μ is the fluid viscosity, σ is the surface tension coefficient, κ is the interface curvature, $\mathbf{n}$ is the unit normal vector to the interface, $\mathbf{g}$ is the gravitational acceleration, and $\delta(\mathbf{x})$ is a delta function that is defined as the product of three one-dimensional delta functions: $\delta(\mathbf{x}) = \delta(x)\delta(y)\delta(z)$, $\mathbf{x} = (x, y, z)$. The subscript f refers to a point on the interface Γ. It is worth pointing out that the material properties density ρ and viscosity μ will be discontinuous across the interface, and there will generally be a jump in the pressure p across the interface as well. Note that the surface tension term is a singular term that only comes into effect on the interface between the two fluids.

We non-dimensionalize the equations by introducing dimensionless characteristic variables as follows:

$$\mathbf{x}^* = \frac{\mathbf{x}}{D}, \quad \mathbf{u}^* = \frac{\mathbf{u}}{\sqrt{gD}}, \quad \tau^* = \sqrt{\frac{g}{D}}t, \quad \rho^* = \frac{\rho}{\rho_{\mathrm{l}}}, \quad p^* = \frac{p}{\rho_{\mathrm{l}}gD}, \quad \mu^* = \frac{\mu}{\mu_{\mathrm{l}}}, \quad \kappa^* = D\kappa, \quad \mathbf{g}^* = \frac{\mathbf{g}}{g},$$

where D is the diameter of a sphere with the same volume as the bubble and $g = \|\mathbf{g}\|$. Thus we may re-express the Navier–Stokes equations as

$$\frac{\partial(\rho\mathbf{u})}{\partial t} + \nabla \cdot \rho\mathbf{u}\mathbf{u} = -\nabla p + \frac{1}{Ar}\nabla \cdot [\mu(\nabla\mathbf{u} + \nabla^{\mathrm{T}}\mathbf{u})] + \frac{1}{Bo}\int_\Gamma \kappa_{\mathrm{f}}\mathbf{n}_{\mathrm{f}}\delta(\mathbf{x} - \mathbf{x}_{\mathrm{f}})\mathrm{d}s + (\rho - 1)\mathbf{g} \tag{3}$$

in which the superscript * has been omitted for convenience. The non-dimensional Archimedes and Bond numbers used here are thus defined as

$$Ar = \frac{\rho_{\mathrm{l}}g^{1/2}D^{3/2}}{\mu_{\mathrm{l}}} \quad \text{and} \quad Bo = \frac{\rho_{\mathrm{l}}gD^2}{\sigma}.$$

The Archimedes number was also used in the previous work [2] to characterize the rise of a bubble in liquid due to buoyancy, reflecting the ratio of buoyancy to viscous forces. By studying the non-dimensional formulation, it can be noticed that the flow is entirely characterized by the following four dimensionless parameters: the density and viscosity ratios of the fluids, the Archimedes number and the Bond number. In experimental work it is common to use a different set of dimensionless numbers [1] – the most important one being the bubble Reynolds number defined as $Re = \frac{\rho_{\mathrm{l}}DU_\infty}{\mu_{\mathrm{l}}}$, where U_∞ is the experimentally measured terminal velocity of the rising bubble. Another dimensionless number one may encounter in this setting is the Froude number, $Fr = U_\infty/(gD)^{1/2}$. We thus have the following relationship between the Archimedes number of our formulation and the Reynolds number used in experiments: $Re = Ar \cdot Fr$. Finally, we mention two other dimensionless numbers frequently used by experimentalists, namely the Eotvos number (E), which is exactly the same as the above-defined Bond number (Bo), and the Morton number $M = \frac{g\mu_{\mathrm{l}}^4}{\rho_{\mathrm{l}}\sigma^3}$.

2.2. Treatment of the discontinuities across the interface

When the governing Navier–Stokes equations are solved numerically on a fixed grid, the values of the density and viscosity on these grid points are required. It is a reasonable assumption that each fluid is incompressible, and fluid properties such as density and viscosity are constant in each fluid phase. Hence the density and viscosity are physically discontinuous across the interface between the two immiscible fluids, and this abrupt jump at grid points adjacent to the interface has traditionally caused great problems in many numerical methods. In Tryggvason et al. [48,47] a fixed background mesh is adopted to solve the governing flow equations, and a separate mesh is applied to track the position of the interface as well as the discontinuities across the front. An illustration of such a mesh system is shown in Fig. 1. The discontinuities across the front are distributed from the front mesh to the background mesh, and continuous distributions of the fluid properties can be reconstructed on the fixed background mesh. The singular source term on the interface is distributed to the background grid similarly, and the governing equations can thus be solved on the fixed background grid using any preferred numerical approach.

The reconstruction of the field distribution $b(\mathbf{x}, t)$ of material properties at time t in the whole domain can be achieved through constructing a certain indicator function $I(\mathbf{x}, t)$. Let this indicator function be zero in the liquid phase and one in the gas phase. We may then define

$$b(\mathbf{x}, t) = b_{\mathrm{l}} + (b_{\mathrm{b}} - b_{\mathrm{l}}) \cdot I(\mathbf{x}, t), \tag{4}$$

where $b(\mathbf{x}, t)$ is either fluid density or viscosity, and the subscripts l and b refer to liquid and gas phase, respectively. Further let Ω be the domain of the gas phase and let Γ be the interface between the two phases. The indicator function may then be expressed as

$$I(\mathbf{x}, t) = \int_{\Omega(t)} \delta(\mathbf{x} - \mathbf{x}')\mathrm{d}\mathbf{x}'. \tag{5}$$

Taking the gradient of the indicator function and applying Stokes' theorem, we get

$$\nabla I(\mathbf{x}, t) = \int_{\Omega(t)} \nabla\delta(\mathbf{x} - \mathbf{x}')\mathrm{d}\mathbf{x}' = \int_{\Gamma(t)} \mathbf{n}\delta(\mathbf{x} - \mathbf{x}')\mathrm{d}s, \tag{6}$$

where $\mathbf{n}$ is the outer unit normal vector of the interface. Taking the divergence yields a Poisson equation for the indicator function:

$$\nabla^2 I(\mathbf{x}, t) = \nabla \cdot \int_{\Gamma(t)} \mathbf{n} \delta(\mathbf{x} - \mathbf{x}') \mathrm{d}s. \tag{7}$$

By solving this equation we obtain the distribution of material properties from Eq. (4). However, this distribution is discontinuous across the front and therefore poses considerable numerical difficulties.

Unverdi and Tryggvason [48] addressed the sharp jump in fluid properties across the interface in their front tracking algorithm. They introduced an artificial thickness of the interface inside which the material properties vary continuously from one fluid to the other. According to this idea, a distribution function $D(\mathbf{x})$ is introduced to approximate the delta function $\delta(\mathbf{x})$ with the assumption of an artificial thickness of the interface. We here adopt the traditional Peskin distribution function [31],

$$D(\mathbf{x} - \mathbf{x}_{\mathrm{f}}) = \begin{cases} (4h)^{-3} \prod_{i=1}^{3} \left(1 + \cos\left(\frac{\pi}{2h}|\mathbf{x}_i - \mathbf{x}_{i,\mathrm{f}}|\right)\right) & \text{if } |\mathbf{x}_i - \mathbf{x}_{i,\mathrm{f}}| < 2h, \\ 0 & \text{otherwise.} \end{cases} \tag{8}$$

Replacing the delta function in Eq. (7) by the above Peskin distribution, an alternative, smooth indicator function can be reconstructed by solving the modified Poisson equation. This indicator function will then be zero in the liquid phase, vary continuously from zero to one in the artificial thickness region, and one in the gas phase.

Besides the discontinuity in fluid properties across the bubble interface, the surface tension, $F_\sigma = \int_\Gamma \sigma_{\mathrm{f}} \kappa_{\mathrm{f}} \mathbf{n}_{\mathrm{f}} \delta(\mathbf{x} - \mathbf{x}_{\mathrm{f}}) \mathrm{d}s$, a singular source term on the bubble interface, represents another great challenge for numerical methods in multiphase flow. In the current study the net force caused by surface tension on the surface elements is calculated, thus circumventing the high-order derivatives involved in curvature calculations. Fig. 2 shows the surface tension force exerted on a central surface element (E_0) by its neighboring elements (E_1, E_2 and E_3). The surface tension force acting on an edge shared between the central element and a neighboring element can be calculated by

$$\mathbf{F}_i = \sigma(\mathbf{t}_i \times \mathbf{n}_{i,0}), \quad i = 1, 2 \text{ and } 3, \tag{9}$$

where $\mathbf{t}_i$ is the vector of edge i and $\mathbf{n}_{i,0}$ is a unit outward normal of edge i. The $\mathbf{n}_{i,0}$ can be estimated by averaging the element normal vectors of the two neighboring elements with the shared edge i. Hence, for a central element E_0, the net force caused by surface tension can be expressed as
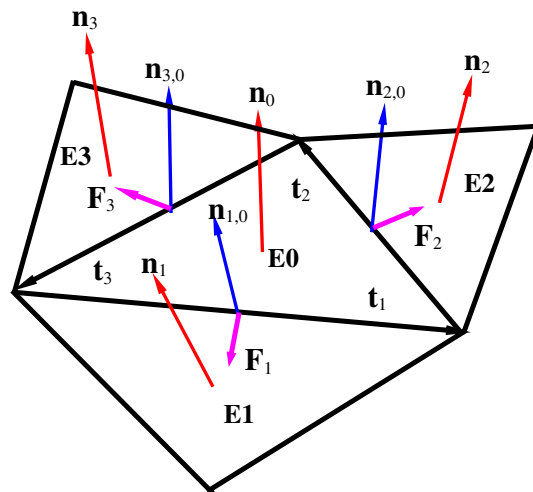

Fig. 2. The surface tension forces ($\mathbf{F}_1$, $\mathbf{F}_2$ and $\mathbf{F}_3$) exerted on a central surface element (E_0) by the neighboring elements (E_1, E_2 and E_3). Here $\mathbf{n}_1$, $\mathbf{n}_2$ and $\mathbf{n}_3$ represent the normal of element E_1, E_2 and E_3, respectively, while $\mathbf{n}_{1,0}$, $\mathbf{n}_{2,0}$ and $\mathbf{n}_{3,0}$ is the normal on the three edges of element E_0, respectively. Further, $\mathbf{t}_1$, $\mathbf{t}_2$ and $\mathbf{t}_3$ indicate the three edge vectors of element E_0.

$$\mathbf{F}_{\sigma,E} = \sum_{i=1}^{3} \mathbf{F}_i = \sigma \sum_{i=1}^{3} (\mathbf{t}_i \times \mathbf{n}_{i,0}). \tag{10}$$

According to Eq. (10), the net surface tension force on all surface elements can be calculated and then distributed to the background mesh for solving the momentum equations:

$$\mathbf{F}_{\sigma}(\mathbf{x}) = \sum_{k} \mathbf{F}_{\sigma,E} D(\mathbf{x} - \mathbf{x}_k). \tag{11}$$

Here $\mathbf{x}_k$ represents the mass centre of the k-th element used to triangulate the bubble surface.

2.3. Tracking the moving interface

With the techniques introduced in Sections 2.1 and 2.2, the governing equations can be solved on a fixed background grid to obtain the flow field. An adaptive, unstructured triangular mesh (front markers) is used to represent the interface between the two fluid phases. The velocity $\mathbf{u}_f(\mathbf{x}_f, t)$ of these moving front markers may then be obtained by interpolation from the flow field on the background mesh. Subsequently, the front mesh points can be advected in a Lagrangian manner from a position $\mathbf{x}_f^n$ at the nth time step to a position $\mathbf{x}_f^{n+1}$ at the $(n+1)$th time step. Thus the front moves with the same velocity as the surrounding fluid, and the so-called no-slip condition of the interface is satisfied. In this paper, the interpolation is carried out using the same distribution function as the one used for the transfer of fluid properties to the background grid, yielding

$$\mathbf{u}_f(\mathbf{x}_f, t) = \sum_{\mathbf{x}} \mathbf{u}(\mathbf{x}, t) D(\mathbf{x} - \mathbf{x}_f), \tag{12}$$

$$\mathbf{x}_f^{n+1} = \mathbf{x}_f^n + \mathbf{u}_f^n \Delta t. \tag{13}$$

As the front marker points are advected, the mesh size and quality may consequently change. The resolution of the front mesh has a strong effect on the information exchange with the fixed background grid, which may eventually affect the accuracy of the simulation results. Therefore, it is of key importance that the front mesh has a more or less constant quality and uniform resolution throughout the duration of the simulation. In this study, the resolution of the triangular mesh for the 3D surface of the bubble is maintained more or less uniform through adaptation as the interface evolves.

2.4. Mesh adaptation

As two sets of mesh are applied in the current front tracking method, the resolution of both the front mesh and the background mesh near the front plays an important role in resolving the interfacial physics of the multiphase flow. From physical principles it is known that fluid particles on the bubble interface will move downwards along the surface towards the bottom of the bubble as it rises. In the front tracking simulation, the mesh points on the bubble interface also move in a similar pattern. As a result, the mesh on the upper part of the bubble becomes coarser. On the other hand, the mesh at the lower part of the bubble becomes increasingly dense. Fig. 3(a) shows the variation of front mesh quality as the bubble rises in liquid without front mesh adaptation. It is obvious that the accuracy will be affected when the mesh on the top is too coarse, and that the dense fine mesh at the bottom of the bubble will consume excessive computing power without much benefit in accuracy. Thus, the front mesh adaptation as shown in Fig. 3(b) is essential to ensure the accuracy and efficiency of the simulation.

In this aspect, three basic operations are adopted to adapt the front mesh, namely edge swap, edge split and edge deletion. For long edges, the edge swap operation as shown in Fig. 4(a) is a simple and easy operation to improve the mesh quality. In the edge split operation as shown in Fig. 4(b), a new point is generated by surface fitting of the existing neighboring mesh points. This new point is then inserted into the two associated meshes, and new and finer triangles are generated to replace the old ones. Thus edge split is important to refine the front mesh. For the deletion of short edges as shown in Fig. 4(c), the triangles associated with the short edge will be deleted, and the resulted gap will be sealed through merging the old nodes of the short edge. Hence, edge deletion is important to coarsen the front mesh. In addition, consistent checking of the mesh connectivity is also important to ensure the accuracy in calculating the surface tension.
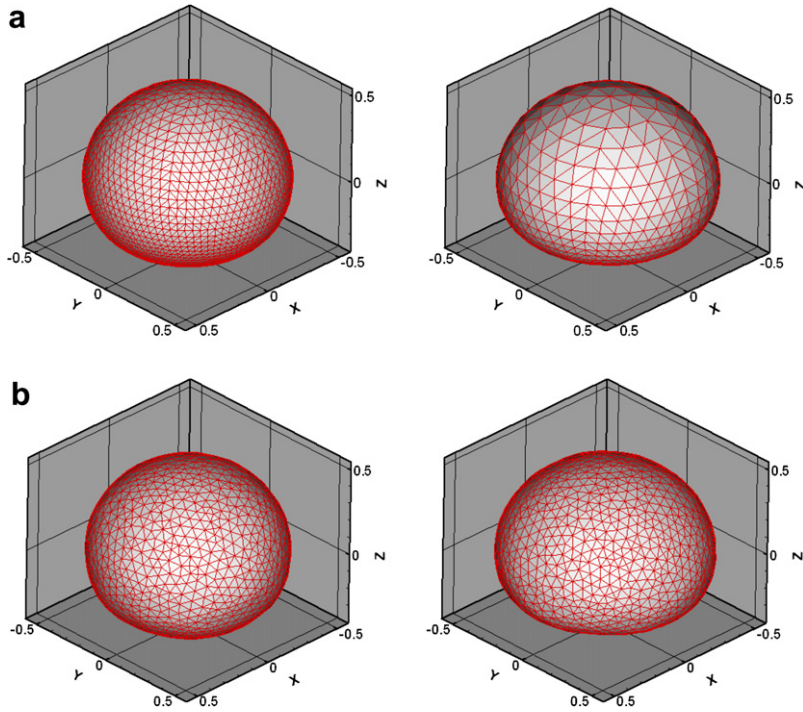
Fig. 3. The evolution of the rising bubble shape at two different time steps and the variation of bubble surface mesh quality (a) without and (b) with adaptation.
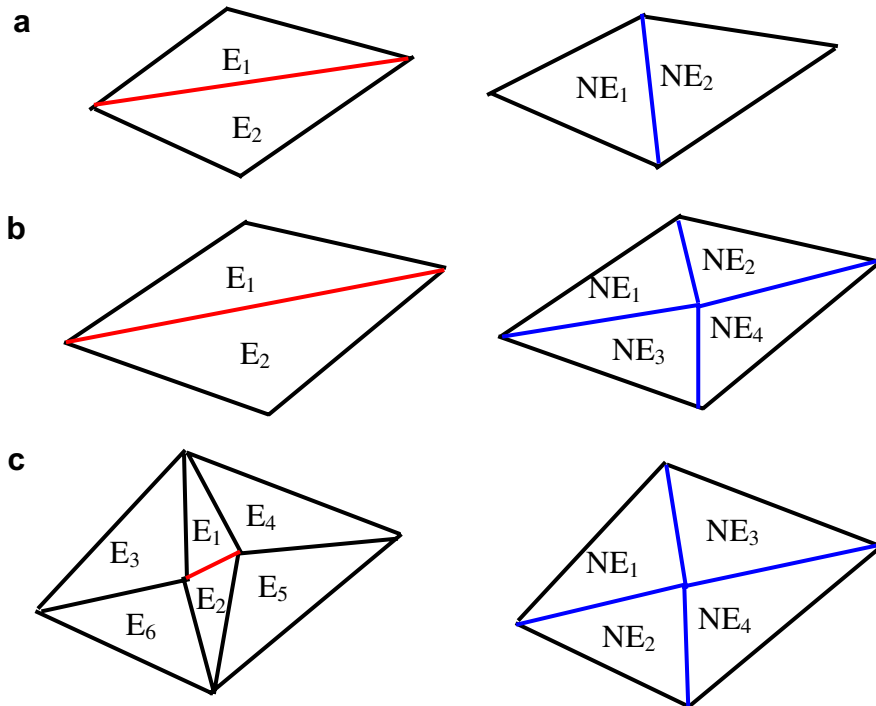

Fig. 4. Basic operations (a) edge swap (b) edge split (c) edge delete for the triangular mesh adaptation of the bubble surface mesh. E stands for existing element to be removed and NE for the new element to be created.

Accordingly, the resolution of the background mesh also plays an important role in capturing the flow behavior – particularly so in the vicinity of the interface. If the background mesh resolution is too low, then the detailed flow dynamics will not be captured reasonably well, resulting in unreliable and inaccurate simulations. Therefore, it is desirable to have relatively high-resolution grids, particularly near the interface, while coarse grids may be used away from the interface. This is achieved in our model by the use of the block-based adaptive mesh refinement (AMR) tool PARAMESH [24]. In this study, the refining and coarsening of the grid blocks is based on whether there exists a bubble front within the blocks. An example of the block-wise Cartesian mesh refinement generated by PARAMESH is showed in Fig. 5. It can be seen that fine background grids are located in the vicinity of the bubble, while coarser background grids are applied in regions further away from the bubble front. This feature makes it more efficient to solve the governing equations and to capture the flow physics near the interface accurately. Another excellent feature of PARAMESH is that all blocks of Cartesian grid points have the same structure at any level of refinement. Hence, once the flow solver is developed for one grid block, it can be easily applied to all other blocks independent of the level of refinement. In addition, the different blocks can be distributed to different CPUs in an MPI parallel environment, which speed up the problem solving cycle.

2.5. Flow solver

The numerical method for the governing flow equations is one of the key components in the simulation. Traditionally, an explicit projection–correction method based on second-order central differences on a regular, staggered Cartesian grid has been used along with the front tracking approach [48]. However, it seems that this approach is unable to handle the large density ratios typical of systems in industrial applications as well as in nature. In search of a more robust solver, Hua and Lou [17] implemented a modified version of the classical SIMPLE method [30] for axisymmetric multiphase flow. Further details about the modified SIMPLE algorithm can be found in the past works [17,6]. Computational results indicate that this approach is more robust than the projection–correction method – especially for multiphase flows with large density ratios such as the air–water system. This improvement is most probably due to the fact that the SIMPLE algorithm avoids solving the problematic pressure equation directly. Instead, the pressure and the velocity are corrected iteratively based on the governing equations.

2.6. Moving reference frame

In many applications of multiphase flow it is often desirable to study the long-term behavior and evolution of the moving interface between the fluids. In such applications the front may move a considerable distance, and the study of the rise path of an air bubble in water is a typical example. The computational domain must then be correspondingly large to accommodate such extensive movement. However, in a three-dimensional
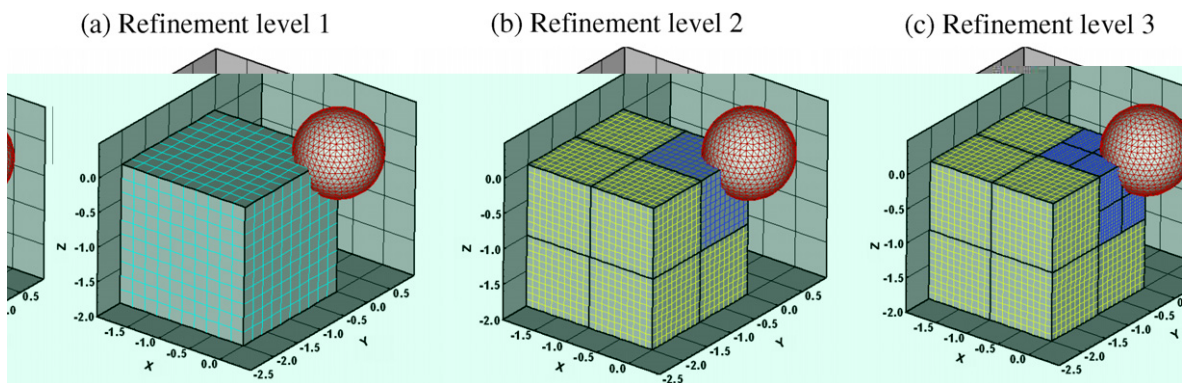

Fig. 5. An illustration of the mesh refinement at different levels for a background block mesh based on the position of the bubble surface. After refinement, the parent block is divided into eight sub-blocks. Each sub-block has the same Cartesian mesh as the parent block.

model with a high-resolution grid, a large computational domain is computationally very expensive. Computational cost may therefore limit the domain size and thus also long-time simulations.

To remedy this problem, we have therefore incorporated a moving reference frame into our numerical algorithm. The idea is to move the reference frame together with the front such that the front (e.g. a bubble) remains more or less fixed in the computational domain. The size of the computational domain may then be chosen independently of the duration of the simulation, and this will in turn reduce the computational cost significantly. As a result, we may carry out long-time simulations of moving interface problems which could not have been done in a stationary reference frame.

Fig. 6 illustrates a moving reference frame. There, the frame XY stands for a stationary reference frame and the frame $X'Y'$ for a moving reference frame. The positions of a monitoring point in the frames XY and $X'Y'$ are represented as $\mathbf{x}_p$ and $\mathbf{x}'_p$, respectively, which are correlated with the position of the moving reference frame ($\mathbf{x}_m$) according to Eq. (14). The velocity of the monitoring point P is $\mathbf{u}(\mathbf{x}, t)$ in the frame XY and $\mathbf{u}'(\mathbf{x}', t)$ in the moving frame $X'Y'$, and the velocity of the moving frame is $\mathbf{u}_m(t)$. The following correlations can be obtained:

$$\mathbf{x}_p = \mathbf{x}_m + \mathbf{x}'_p, \tag{14}$$

$$\mathbf{u}(\mathbf{x}, t) = \mathbf{u}_m(t) + \mathbf{u}'(\mathbf{x}', t). \tag{15}$$

Allowing translational, but not rotational, movement of the frame in the present study, the following is the updated governing flow equations in the moving reference frame:

$$\frac{\partial(\rho \mathbf{u}')}{\partial t} + \nabla' \cdot \rho \mathbf{u}' \mathbf{u}' + \rho \frac{\mathrm{d}\mathbf{u}_m}{\mathrm{d}t} = -\nabla' p + \frac{1}{Ar} \nabla' \cdot [\mu(\nabla' \mathbf{u}' + \nabla'^{\mathrm{T}} \mathbf{u}')] + \frac{1}{Bo} \int_{\Gamma} \kappa_f \mathbf{n}_f \delta(\mathbf{x}' - \mathbf{x}'_f) \mathrm{d}s + (\rho - 1)\mathbf{g}, \tag{16}$$

$$\nabla' \cdot \mathbf{u}' = 0. \tag{17}$$

The moving front will generally be accelerating and so will the moving reference frame. Thus the frame of reference in which we solve the governing equations is no longer an inertial frame, and we must therefore modify the momentum equations to take into account the acceleration of the frame. In addition, according to Eq. (15), when the governing equations are solved in a moving reference frame, the velocity condition on the boundary ($\mathbf{x}'_B$) should be modified as $\mathbf{u}'(\mathbf{x}'_B, t) = \mathbf{u}(\mathbf{x}_B, t) - \mathbf{u}_m(t)$.
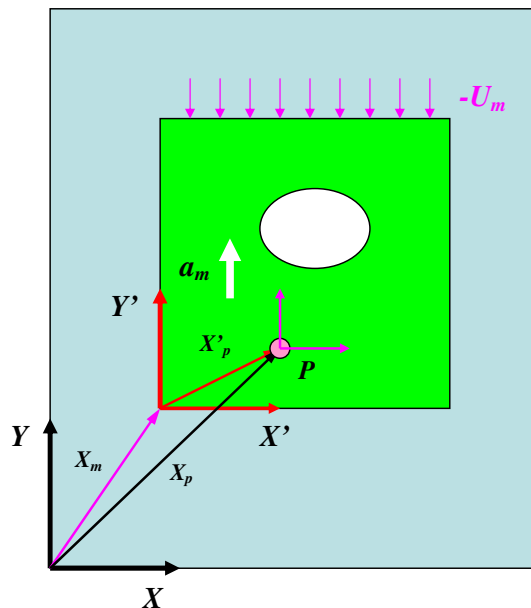

Fig. 6. Schematic diagram showing the implementation of a moving reference frame attached to the rising bubble. Frame XY represents a stationary frame and Frame $X'Y'$ a moving frame. P is a point associated with the bubble surface where the moving frame is to be attached.

Notice that the additional term on the left-hand side $d\mathbf{u}_m/dt$, which denotes the acceleration $\mathbf{a}_m$ of the moving reference frame, is added in Eq. (16). We aim to choose $\mathbf{a}_m$ so that the rising bubble remains as fixed as possible in the moving frame, i.e. ideally the acceleration of the frame is equal to the acceleration of the bubble. The bubble acceleration is of course unknown, so we need to approximate this acceleration at each time step. We shall adopt the prediction as presented by Rusche [36], namely

$$\mathbf{a}_m^{n+1} = -\frac{\Delta\mathbf{u}_m^{n+1}}{(\Delta t)^n}, \tag{18}$$

where

$$\Delta\mathbf{u}_m^{n+1} = \lambda_1 \frac{\mathbf{x}_d^0 - \mathbf{x}_d^n}{(\Delta t)^n} - \lambda_2 \frac{\mathbf{x}_d^n - \mathbf{x}_d^{n-1}}{(\Delta t)^n}. \tag{19}$$

Here $\mathbf{x}_d^j$ is the position of the bubble mass centre relative to the moving frame at time step j, $(\Delta t)^n = t^n - t^{n-1}$, and λ_1 and λ_2 are appropriate under-relaxation factors. It was found that $\lambda_1 = \lambda_2 = 0.1$ gave good results in the present study.

2.7. Boundary conditions

One aim of the current study is to investigate the dynamics of a single bubble rising in liquid. This system has been extensively studied experimentally, and can therefore be used as a good study case to validate the current numerical modeling algorithm. In experiments, the bubble rises in a liquid tank which is typically much larger than the bubble size (about 20 bubble diameters) to minimize the tank wall effect. In the present simulations, the side length of the cubic simulation domain is selected to be eight times the bubble diameter, which is large enough to neglect wall containment effects as concluded in the domain size sensitivity analysis presented in Section 3.1. In addition, free slip boundary conditions are applied on the four vertical walls of the cubic simulation domain. A pressure inlet boundary condition is applied on the top of the computational domain. Here the pressure is fixed to be zero, the vertical velocity component has a zero normal gradient, and the horizontal velocity components are assumed to be zero. A velocity outflow boundary condition is applied on the bottom of the simulation domain, where the flow velocity is set to be the moving speed of the reference frame and zero normal gradient condition is applied to the pressure. The moving speed for the stationary reference frame is set to be zero, while the speed for the moving reference frame can be calculated according to the method introduced in the previous section.

2.8. Solution procedure

We may now summarize the main steps in advancing the solution from one time step to the next as follows:

(1) The velocity of the front marker points, $\mathbf{u}_f^n$, is calculated through interpolation of the fluid velocity field $\mathbf{u}^n$ according to Eq. (12).
(2) The front is advected to its new position $\mathbf{x}_f^{n+1}$ by using the interface velocity $\mathbf{u}_f^n$ found in step (1) – see Eq. (13). The front elements are then subject to examination for adaptation and topological change. Meanwhile, volume conservation is enforced.
(3) The indicator function $I^{n+1}(\mathbf{x}_f^{n+1})$ is computed based on the interface position $\mathbf{x}_f^{n+1}$. This is done by solving the Poisson problem in Eq. (7) with the discrete delta distribution from Eq. (8). Subsequently, the distribution of the density ρ^{n+1}, the viscosity μ^{n+1} and the surface tension $\mathbf{F}_\sigma^{n+1}$ is updated on the flow solver grid points.
(4) We find the velocity field $\mathbf{u}^{n+1}$ and the pressure p^{n+1} by solving the mass continuity and momentum equations using a modified version of the SIMPLE algorithm. Appropriate boundary conditions are applied according to Section 2.7.
(5) Repeat steps (1)–(4) to advance the solution to time t^{n+2}.

3. Results and discussion

In this section, we report various numerical results serving different purposes: model sensitivity analysis, experimental validation, and also model capabilities exploration. A summary of all the simulations can be found in Table 1, in which all simulation parameters are listed.

3.1. Sensitivity analysis – size of the computational domain

Extensive experiments have been performed in the past to study the rise and deformation of a single bubble in quiescent liquids. Often these experiments have been done in large containers with a size of at least 20 bubble diameters in each spatial direction to avoid wall containment effects [1]. In this paper, we intend to validate simulation results against such experiments. To achieve this, the computational domain should also be rather large to avoid any significant effects caused by the wall confinement. On the other hand, if the domain is chosen too large, excessive computing time is needed to complete the simulation. To analyze the influence of the domain size, a number of numerical tests were run with domain sizes ranging from 2 to 12 bubble diameters in each of the spatial dimensions. The grid resolution was kept constant and accommodated approximately 20 cells inside the bubble in each direction. All computations were carried out in a moving reference frame.

The terminal rise velocity and the terminal bubble shape were used to assess the wall confinement effects for various domain sizes. The aim of this sensitivity analysis was to find the smallest possible computational domain in which wall containment effects have negligible impact on the bubble terminal velocity and shape. Fig. 7 presents the simulation results of the terminal bubble shape and the rise velocity using different domain sizes under the conditions of $Bo = 243.0$, $Ar = 15.24$, $\rho_l/\rho_b = 1000$ and $\mu_l/\mu_b = 100$ (Case A3). There is a notable change in the terminal bubble shape and rise velocity as the domain size is increased from two to six bubble diameters. When the domain size is increased beyond six bubble diameters, no significant change in the simulation results is observed. Moreover, it is noted that the wall confinement has a strong effect on the terminal velocity for small domain sizes from two to six bubble diameters. However, the change in terminal velocity is only around 1% when increasing the computational domain size from 8 to 10 bubble diameters in each spatial dimension. Based on these observations we conclude that a domain size with side length of eight bubble diameters should be sufficient in our simulations. Actually, experimental results by Krishna et al. [23] also indicate that wall effects on a rising bubble is negligible when the diameter of the liquid container is eight bubble diameters or larger.

3.2. Sensitivity analysis – grid resolution

PARAMESH divides the computational domain into a number of blocks in each spatial direction. Each block consists of a certain number of grid cells in each direction, and the governing equations are discretized and solved numerically on these grid cells. For a computational domain of fixed size, there are therefore two ways to change the grid resolution using PARAMESH: either by changing the number of blocks, which is determined by the maximum number of refinement levels, or by changing the number of cells in each block.

Table 1
The physical parameters for the various test cases reported in this paper

Test case	Ar	Bo	ρ_l/ρ_b	μ_l/μ_b
A1	1.671	17.7	1000	100
A2	79.88	32.2	1000	100
A3	15.24	243	1000	100
A4	134.6	115	1000	100
A5	30.83	339	1000	100
B1	134.6 (large bubble)	115.0 (large bubble)	1181	5000
	47.6 (small bubble)	28.75 (small bubble)		
B2	15.24 (large bubble)	243.0 (large bubble)	1181	5000
	5.38 (small bubble)	60.75 (small bubble)		

a

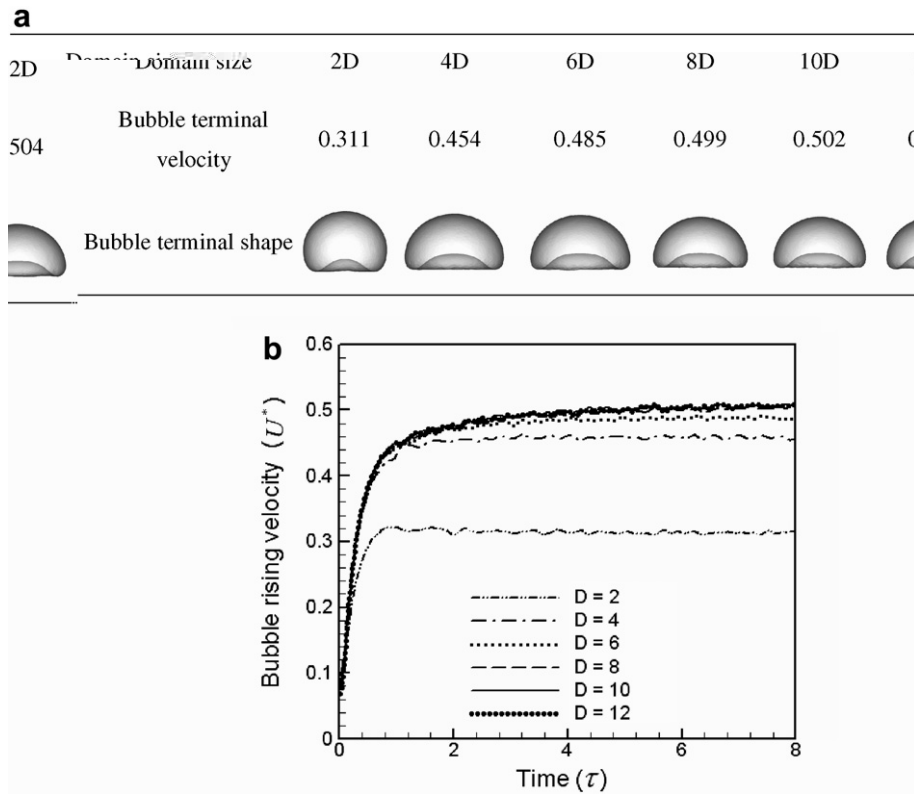| Domain size	2D	2D	4D	6D	8D	10D	1
Bubble terminal velocity	504	0.311	0.454	0.485	0.499	0.502	0
Bubble terminal shape							

Fig. 7. Sensitivity analysis about the effects of the computational domain size on (a) the bubble shape and (b) the bubble rising velocity predicted in the simulation under the conditions of $Ar = 15.24$, $Bo = 243.0$, $\rho_l/\rho_b = 1000$ and $\mu_l/\mu_b = 100$. Here, D in figure (b) is the side length of the cubic computational domain measured in number of bubble diameters.

In our grid sensitivity analysis we kept the maximum refinement level fixed and changed the number of cells in each block. All simulations were done in a moving, cubic computational domain with side length equal to eight bubble diameters using equal grid spacing in each of the spatial directions.

The results from the grid sensitivity analysis can be found in Fig. 8 under the conditions of $Bo = 243.0$, $Ar = 15.24$, $\rho_l/\rho_b = 1000$ and $\mu_l/\mu_b = 100$ (Case A3). It is noted that the terminal bubble velocity is highly sensitive to the mesh resolution up until 16 cells per bubble in each space direction. However, increasing the number of cells from 16 to 20 yields less than 1% change in terminal velocity. The terminal bubble shape also has a very strong dependence on the grid resolution – especially when the grid resolution is relatively low. On the other hand, we can even see a slight change in shape when we increase the number of cells per bubble diameter from 16 to 20. However, increasing the number of cells per bubble diameter further to 32 does not lead to any visually detectable change in the bubble shape. Based on the above we find it sufficient to use a resolution of 20 cells per bubble diameter in our simulations.

3.3. Comparison of results obtained in a stationary and a moving reference frame

Since a moving reference is introduced in this paper to perform long-time simulations of both single bubble rising and two bubbles interacting, it is important to evaluate the accuracy and impact of using a moving reference frame as opposed to a stationary frame. For this purpose, simulation results for Case A4 obtained in a stationary reference frame are compared with those obtained in a moving reference frame.

The bubble shapes predicted in both stationary and moving frames at different time steps are shown in Fig. 9. A closer look at this figure shows that the differences between the shapes obtained in the two reference frames are negligible. A comparison of the velocity profiles of bubbles rising in a stationary and a moving ref-

a

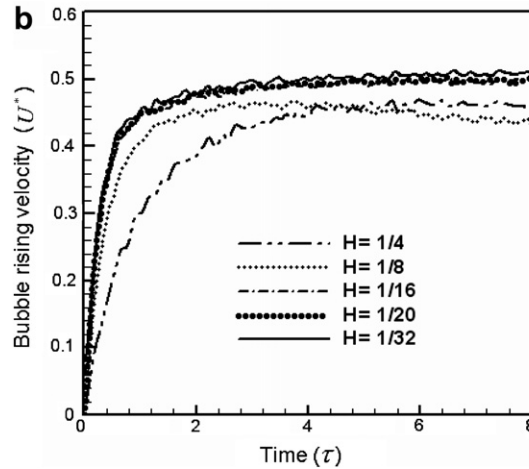| Number of background grid per bubble	4	8	16	20	32
Terminal bubble velocity	0.311	0.454	0.485	0.499	0.502
Terminal bubble shape					

b

Fig. 8. Sensitivity analysis about the effects of background grid size on (a) the bubble shape and (b) the bubble rising velocity predicted in the simulation under the conditions of $Ar = 15.24$, $Bo = 243.0$, $\rho_l/\rho_b = 1000$ and $\mu_l/\mu_b = 100$. Here, H in figure (b) stands for the ratio of grid size to bubble diametre.
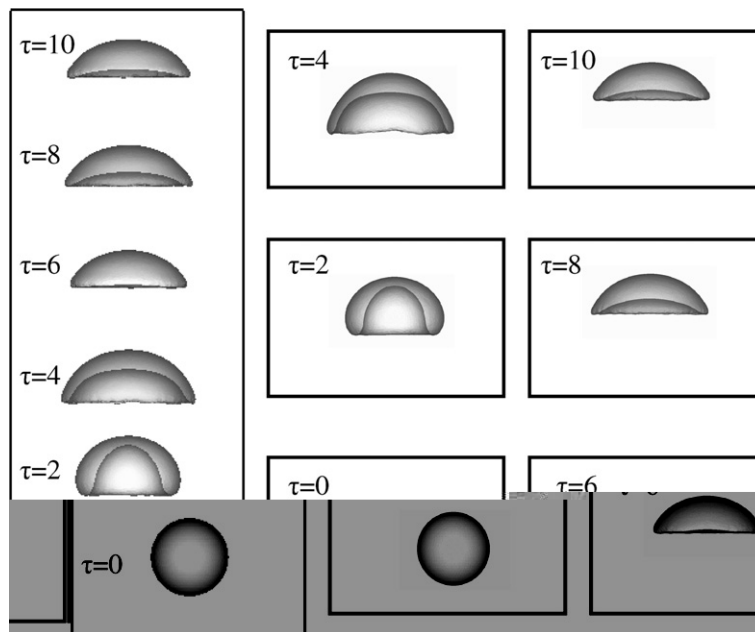
Fig. 9. A comparison of the evolution of the predicted bubble shapes in a stationary (the left-most column) and a moving reference frame (the two right-most columns) under the conditions of $Ar = 134.6$, $Bo = 115.0$, $\rho_l/\rho_b = 1000$ and $\mu_l/\mu_b = 100$.

erence frame is shown in Fig. 10, and they are in reasonable agreement. Note that the velocity of the moving frame has been added to the rise velocity obtained in the moving reference frame to enable a direct comparison with the rise velocity in the stationary frame. In addition to comparing bulk behavior of rising bubbles, we would also like to compare the detailed flow patterns around the bubbles.

A comparison of the streamlines predicted in a stationary and a moving frame can be found in Fig. 11. Since one frame is at rest and one is moving, comparing streamlines would only be sensible if we modify the velocity in one of the frames to account for the different velocities of the frames. Here we have chosen to subtract the velocity of the moving reference frame from the velocity field computed in the stationary frame before comparison. It can be seen from Fig. 11 that an excellent agreement of the streamline patterns in the stationary and the moving frame is obtained. Furthermore, pressure distributions predicted in a stationary and a moving frame are compared in Fig. 12, and again the results agree well.

Based on the various tests and comparisons of different flow characteristics carried out and described above, we can conclude that the use of a moving reference frame yields numerical results in reasonable agreement to those obtained in a stationary reference frame.
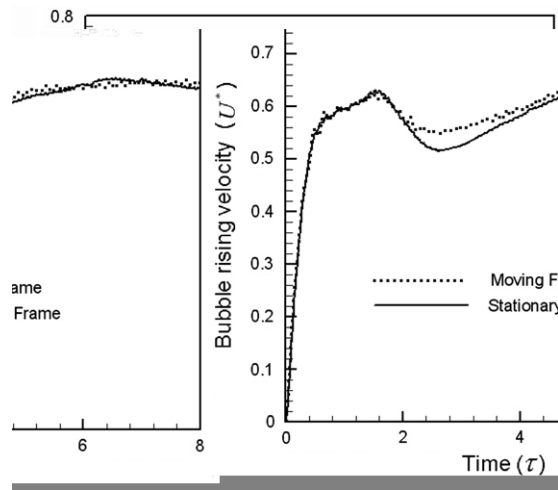

Fig. 10. A comparison of the bubble rise velocities predicted in a stationary and a moving reference frame under the conditions of $Ar = 134.6$, $Bo = 115.0$, $\rho_l/\rho_b = 1000$ and $\mu_l/\mu_b = 100$.
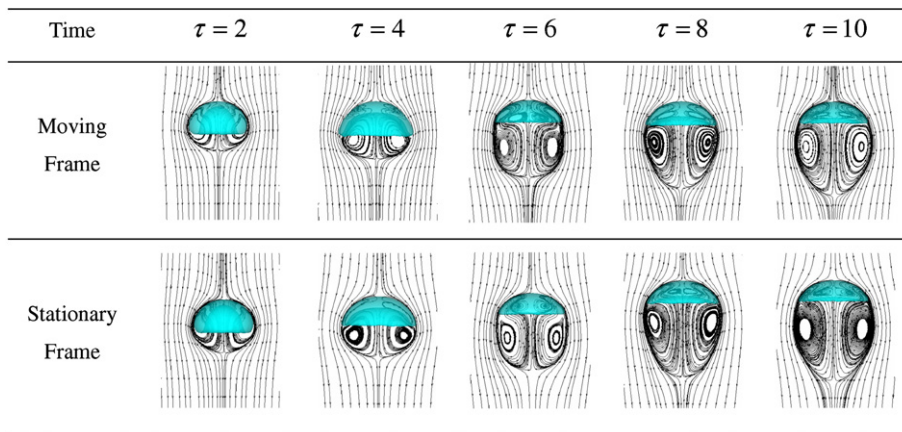

Fig. 11. Comparison of flow streamlines near the bubble at different times computed in a stationary and a moving frame under the conditions of $Ar = 134.6$, $Bo = 115.0$, $\rho_l/\rho_b = 1000$ and $\mu_l/\mu_b = 100$. To enable a direct comparison, the velocity of the moving frame was subtracted from the velocity computed in the stationary frame.
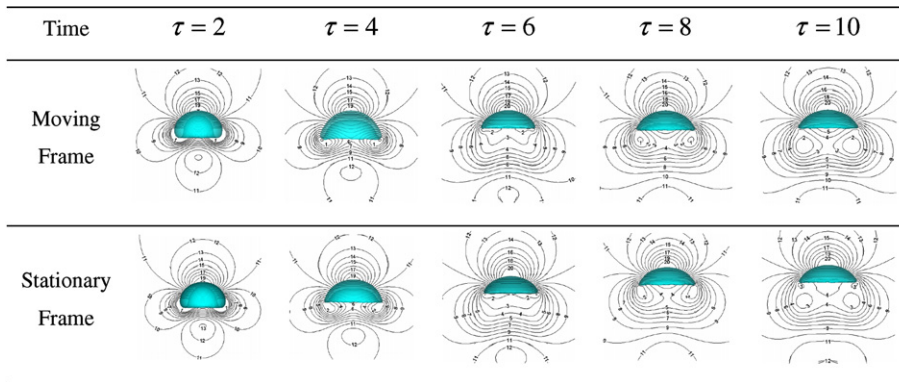
Fig. 12. Comparison of pressure distributions near the bubble at different times computed in a stationary frame and a moving frame under the conditions of $Ar = 134.6$, $Bo = 115.0$, $\rho_l/\rho_b = 1000$ and $\mu_l/\mu_b = 100$.

3.4. Model validation with experiments

In this section, we will compare experimental results available in the literature [1] with predictions obtained by our numerical method. In Fig. 13, we compare observed and predicted terminal bubble shapes for a range of Reynolds and Bond numbers, and the results agree very well. Table 2 shows a comparison of the associated terminal rise velocities, and again there is reasonable agreement between experiments and our numerical predictions. However, it is noted that the relative deviation in Case A1 is a little bit high as the numerically predicted Reynolds number is about 20% lower than that observed in experiments. This deviation may be due to the low rise velocity where the relative error will be high even for small absolute errors though there is no

Test Case	Experiments			Simulations	
	Test Conditions	Observed terminal bubble shape		Predicted terminal bubble shape	Modeling conditions and predicted terminal velocity
A1	E = 17.7 M = 711 Re = 0.232				Bo = 17.7 Ar = 1.671 Fr = 0.109
A2	E = 32.2 M = 8.2x10^{-4} Re = 55.3				Bo = 32.2 Ar = 79.88 Fr = 0.686
A3	E = 243 M = 266 Re = 7.77				Bo = 243 Ar = 15.24 Fr = 0.499
A4	E = 115 M = 4.63x10^{-3} Re = 94.0				Bo = 115 Ar = 134.6 Fr = 0.666
A5	E = 339 M = 43.1 Re = 18.3				Bo = 339 Ar = 30.83 Fr = 0.576

Fig. 13. Comparison of terminal bubble shapes observed in experiments [1] and predicted by numerical simulations.

Table 2
Comparison of terminal rise velocities found in experiment [1] and predicted by numerical simulations

Test cases	Experiment	Simulation			Deviation
	Re	Ar	Fr	$Re_c = Fr \cdot Ar$	$\lvert Re - Re_c \rvert / Re \cdot 100$
A1	0.232	1.671	0.109	0.182	21.49
A2	55.3	79.88	0.686	54.798	0.91
A3	7.77	15.24	0.499	7.605	2.13
A4	94.0	134.6	0.666	89.644	4.63
A5	18.3	30.83	0.576	17.758	2.96

change in the simulation accuracy. Another possible reason is that the hindrance effect due to the limited size of the domain becomes significant at low Reynolds numbers. Since free slip boundary is applied in the current simulation, the computation of a single bubble rising corresponds rigorously to the rise of a homogeneous swarm of bubbles. Sangani [38] calculated the sedimentation velocity of a swarm of spherical bubbles at low Reynolds numbers for a complete range of volume fractions. As the cubic simulation domain has a side length equal to eight bubble diameters ($8D$), the volume fraction of the bubble swarm is $\alpha = 4/3 \cdot \pi(D/2)^3/(8D)^3 \approx 1.023 \times 10^{-3}$. In this case $\alpha \ll 1$, and the velocity of the bubble swarm is given by $U_{\text{swarm}}/U_s = 1 - 1.76\frac{K+2/3}{K+1}\alpha^{1/3}$, where U_s is the velocity of the single bubble, and $K = \mu_b/\mu_l$. Calculations then yield $U_{\text{swarm}}/U_s \approx 0.88$ as $K = 0.01$ for Case A1. Hence, due to the limited size of the computational domain, the estimated bubble swarm velocity is about 12% lower than the velocity of a single free rising bubble. This could explain the discrepancy observed for Case A1.

Air bubbles rising in water are common in many industrial processes. Examples in chemical engineering include bubble columns, loop reactors, agitated stirred reactors, flotation, and fermentation reactors. For the design of efficient two-phase reactors, detailed knowledge of bubble sizes and shapes, slip velocities, internal circulations, swarm behaviors, bubble induced turbulence and mixing, and bubble size distributions (including coalescence and breakup) is of fundamental importance. In such industrial applications, bubbles often have non-spherical and even dynamic shapes as well as asymmetric wake structures. Extensive experimental studies have been performed to study air bubbles rising in water [7,46]. Their measurements of the terminal rise velocity of air bubbles in water are presented in Fig. 14 as a function of the bubble size. It is found that the measured terminal velocity vary significantly (or bifurcation) when the bubble diameter is greater than 0.5 mm and smaller than 10 mm. Traditionally this variation has been explained by the presence of surfactants [7], but more recently both Wu and Gharib [49] and Tomiyama et al. [46] attributed this variation to the man-
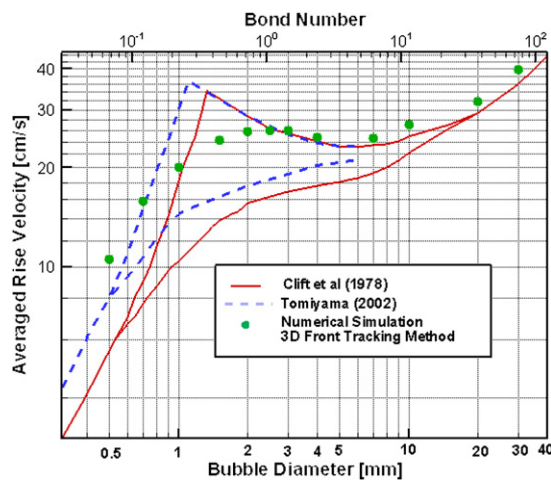

Fig. 14. Comparison of the terminal velocity of air bubbles of different size rising in water predicted in the present simulations and observed in experiments [7,44].

ner in which the initial bubbles were generated. The issue continues to be a matter of discussion – refer to Yang et al. [50].

Due to difficulties in measuring the physical properties on the bubble, a fundamental understanding of the system of a single bubble rising in high Reynolds number regimes is not well established. With the recent rapid increase in computing power, numerical simulations of two-phase flows based on continuum mechanics models with moving free interfaces have become feasible and proved extremely useful for a better understanding of fundamental processes and phenomena. However, numerical modeling of the multi-fluid system of air bubbles rising in water is still quite challenging due to the large density ratio of water to air, the low liquid viscosity of water, high Reynolds numbers, and large bubble deformations. Koebe et al. [21] started early trials of 3D direct numerical simulation of air bubbles rising in water at high Reynolds number using a volume of fluid (VOF) method. They studied bubbles with diameters from 0.5 to 15 mm, and their numerical predictions on the terminal rise velocity of the bubbles agree reasonably with experimental data. However, they introduced some initial white noise in the simulations, which may introduce non-physical perturbations to the simulation system. The recent work by Dijkhuizen et al. [9] reported their trial on simulation of single air bubbles rising in initially quiescent pure water using both a 3D front tracking method and a 2D VOF method for bubble diameters ranging from 1 to 8 mm. The calculated terminal rise velocities by the 3D front tracking method are quite close to the experimental observations by Tomiyama et al. [46], but they over-predicted the velocity for bubble diameters larger than 3 mm.

In this paper, we use the front tracking method with features of mesh adaptation and moving reference frame, allowing a finer mesh in the region of the bubble surface. Consequently, better accuracy is obtained in the current simulations. We simulate a single air bubble rising in initially quiescent pure water with bubble diameters ranging from 0.5 to 30 mm. The numerically predicted rise velocities of the bubbles agree well with the upper bound of the experimental measurements by Tomiyama et al. [46] within the whole range of different bubble sizes as shown in Fig. 14. The variation of terminal shape of the rising bubble with a wide range of bubble size from 0.5 to 30 mm is shown in Fig. 15, which has reasonable agreement with experimental observations [7]. When the bubble diameter is in the range from 2.0 to 10 mm, oscillation of the bubble rise velocity and the bubble shape is also predicted in the simulations. The terminal bubble rise velocity is calculated through averaging the instantaneous rise velocity over a period of time. Since we assume the initial bubble
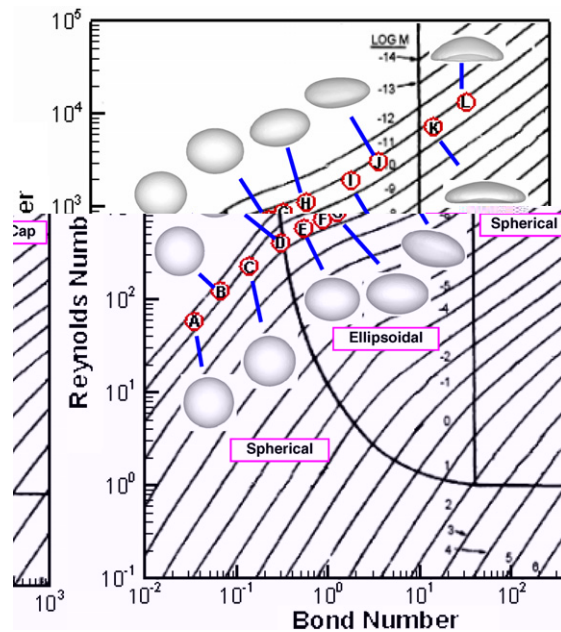

Fig. 15. Numerically predicted terminal shapes of air bubbles rising in water for bubble diameters ranging from 0.5 to 30 mm. The points A to L correspond to the bubble size of 0.5, 0.7, 1.0, 1.5, 2.0, 2.5, 3.0, 4.0, 7.0, 10.0, 20.0 and 30.0 mm, respectively.

shape to be spherical and the surface tension coefficient to be constant, the bifurcation of the bubble rise velocity is not revealed in the current simulation. However, this is an interesting topic to be explored in the future.

3.5. Numerical studies on the interaction between two rising bubbles in viscous liquid

The problem of a single bubble rising in a viscous liquid is an ideal case for numerical model validation. However, the final goal when developing a numerical model for multiphase flow is not just investigating the flow behavior of single bubbles rising in viscous liquids, but also investigating multi-fluid systems with multiple bubbles. With the confidence from validating the current model for a single bubble rising in a viscous liquid, we would like to extend this model to explore the complex interaction between two bubbles rising in a liquid. In the present study, the bubble coalescence criteria is simplified, and only geometrical constraints are considered. This means that bubble coalescence occurs when two points on the bubble surface are close
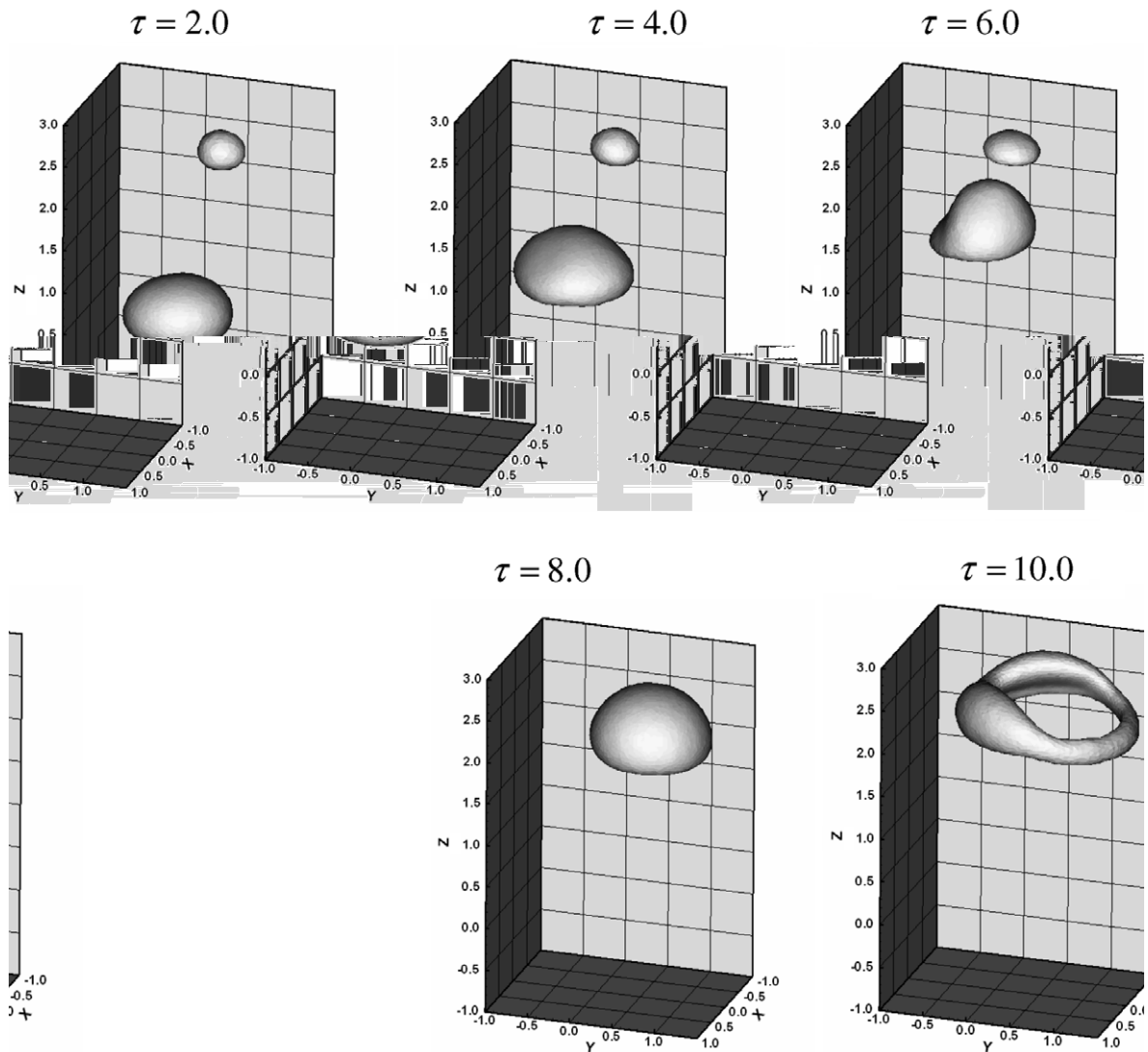

Fig. 16. Numerical simulation of the interaction of two rising bubbles of different size. The flow conditions (Case B1) are: $Ar = 134.6$, $Bo = 115.0$ for the larger bubble and $Ar = 47.6$, $Bo = 28.75$ for the smaller bubble while $\rho_l/\rho_b = 1181$, $\mu_l/\mu_b = 5000$ for both bubbles. The initial diameter of the larger bubble is $D = 1.0$, twice that of the smaller bubble. The smaller bubble is initially located $2.5D$ higher in vertical direction and $0.5D$ axis-off in the Y-direction relative to the larger bubble.

enough, e.g. one fifth of the size of the bubble surface mesh. The topology change associated with the coalescence is maintained from a geometrical point of view. A similar modeling strategy can also been found in the work by Shin and Juric [41]. Figs. 16 and 18 illustrate the simulation of the interaction of two initially spherical bubbles rising in a quiescent liquid due to buoyancy.

In the first simulation, one smaller bubble is initially located $2.5D$ above a bigger bubble in vertical direction, and $0.5D$ axis-off from the bigger bubble in the horizontal direction of Y. Here, D represents the effective diameter of the bigger bubble. The diameter of the smaller bubble is half that of the bigger bubble. The flow conditions for the bigger bubble are as follows: $Ar = 134.6$, $Bo = 115.0$, $\rho_l/\rho_b = 1181$ and $\mu_l/\mu_b = 5000$ (Case B1). Fig. 16 shows the temporal bubble shape evolution of the two rising bubbles. As the bigger bubble has a higher rise velocity, it will catch up with the smaller bubble (Fig. 16 ($\tau = 4.0$)). When they are close enough, the trailing bigger bubble is significantly affected by the low-pressure zone in the wake of the leading smaller bubble. The trailing bubble undergoes large deformations and moves towards the bottom wake zone of the leading bubble (Fig. 16 ($\tau = 6.0$)). Finally, the trailing big bubble merges with the leading smaller bubble, and a toroidal bubble ring is formed (Fig. 16 ($\tau = 10.0$)). Similar bubble shape evolution patterns have also been predicted in other numerical studies [42]. In addition, Fig. 17 shows the temporal variation of the position of the bubbles in both vertical and horizontal directions. It can be seen from Fig. 17(a) that the trailing bigger bubble has a higher rise speed than the smaller leading bubble. The interesting finding is that when the two bubbles are close enough, then the rise speed of both bubbles increases significantly. After the coalescence of the two bubbles, the resulting merged bubble returns to the familiar situation of a single bubble rising. The lateral movement of the trailing bubble caused by the leading bubble can be seen in Fig. 17(b). Even though initially the leading bubble moves slightly away from the trailing bubble laterally, this distance is quite small. However, the trailing bubble, despite its big size, is significantly affected by the leading bubble and moves towards it.

In the second simulation, the smaller bubble is initially located $2.5D$ above the bigger bubble in vertical direction, and $1.0D$ centre-off from the big bubble in the horizontal direction of Y. Here, D represents the effective diameter of the bigger bubble. The diameter of the smaller bubble is half that of the bigger bubble. The flow conditions for the bigger bubble are as follows: $Ar = 15.24$, $Bo = 243.0$, $\rho_l/\rho_b = 1181$ and $\mu_l/\mu_b = 5000$ (Case B2). Fig. 18 shows the temporal evolution of the two rising bubbles. In this case the initial horizontal off-set between the bubbles is larger than in the previous case, and as a result the bigger bubble now actually overtakes the smaller one. It can be seen from Figs. 18 and 19(b) that the leading bubble first starts moving laterally away from the trailing bubble, whereas the trailing bubble then starts moving towards the leading bubble before the overtaking occurs (Fig. 18 ($\tau = 4.0$, $\tau = 6.0$, $\tau = 8.0$)). After the bigger bubble
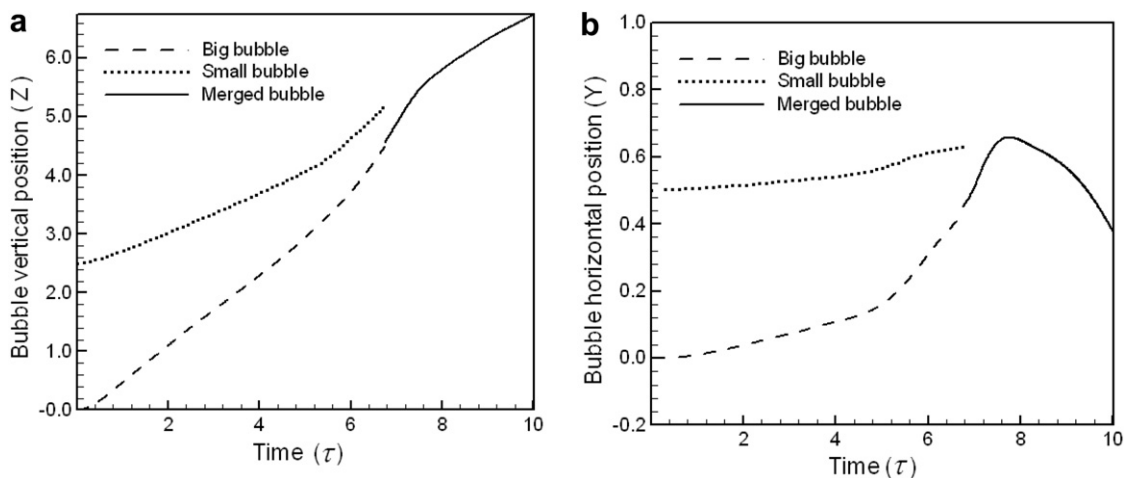

Fig. 17. Simulation predicted (a) vertical and (b) lateral movement in Y-direction of two rising bubbles and the merged bubble under the same conditions as those in Fig. 16.
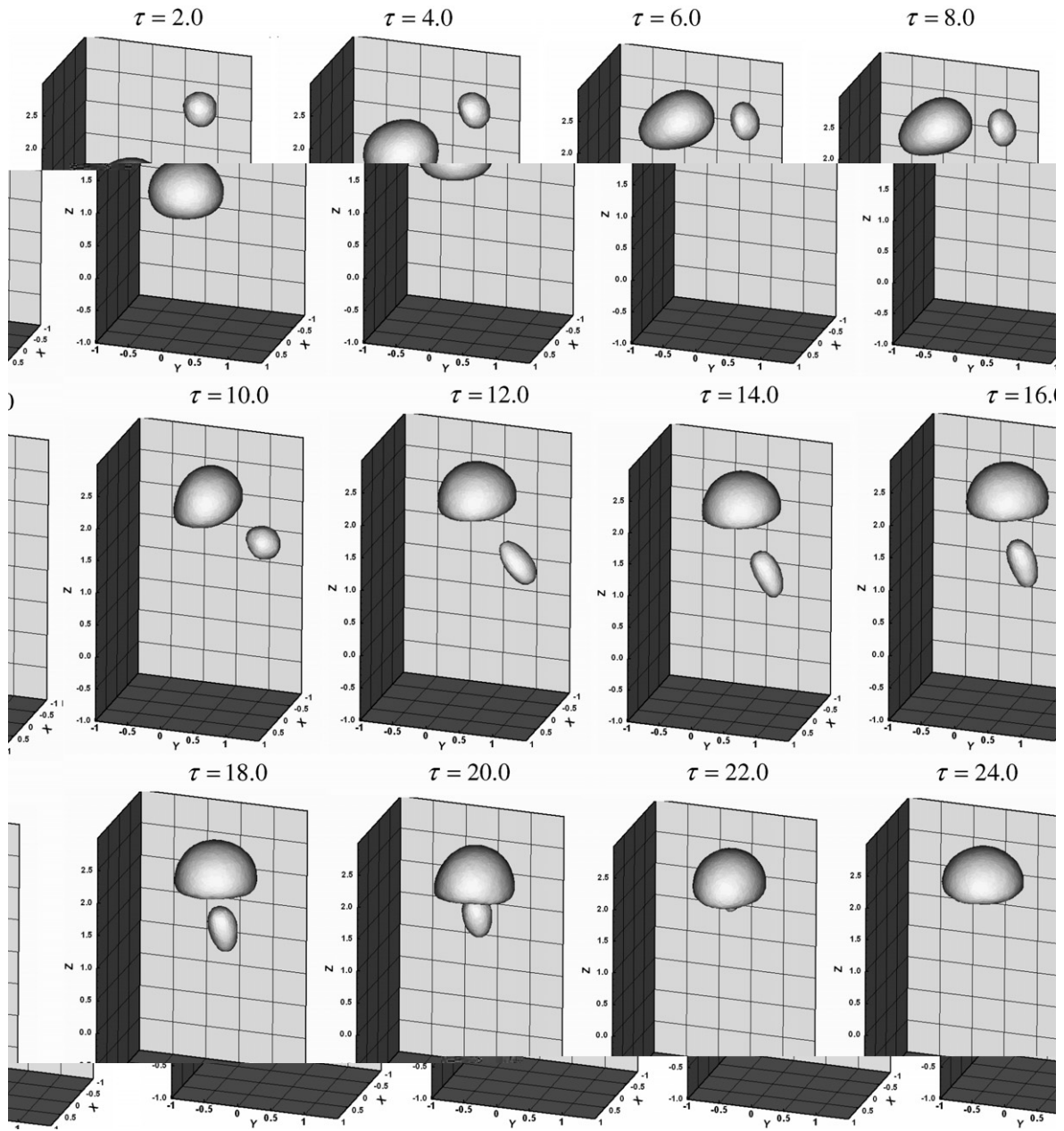
Fig. 18. Numerical simulation of the interaction of two rising bubbles of different size. The flow conditions (Case B2) are: $Ar = 15.24$, $Bo = 243.0$ for the larger bubble and $Ar = 5.38$, $Bo = 60.75$ for the smaller bubble while $\rho_l/\rho_b = 1181$, $\mu_l/\mu_b = 5000$ for both bubbles. The initial diameter of the larger bubble is $D = 1.0$, twice that of the smaller bubble. The smaller bubble is initially located $2.5D$ higher in vertical direction and $1.0D$ centre-off in the Y-direction relative to the larger bubble.

has overtaken the smaller one, the smaller bubble is significantly affected by the wake of the bigger bubble. In fact, the smaller bubble is attracted to the wake of the bigger bubble, resulting in a highly deformed and elongated bubble shape as shown in Fig. 18 ($\tau = 12.0$, $\tau = 14.0$, $\tau = 16.0$). It is also noticed from Fig. 19(a) that the smaller bubble is accelerated and rises fast in the wake of the bigger bubble, and finally, it catches up and merges with the bigger bubble (Fig. 18 ($\tau = 18.0$, $\tau = 20.0$, $\tau = 22.0$)). In this case, the smaller trailing bubble has little effect on the rising speed of the bigger leading bubble.
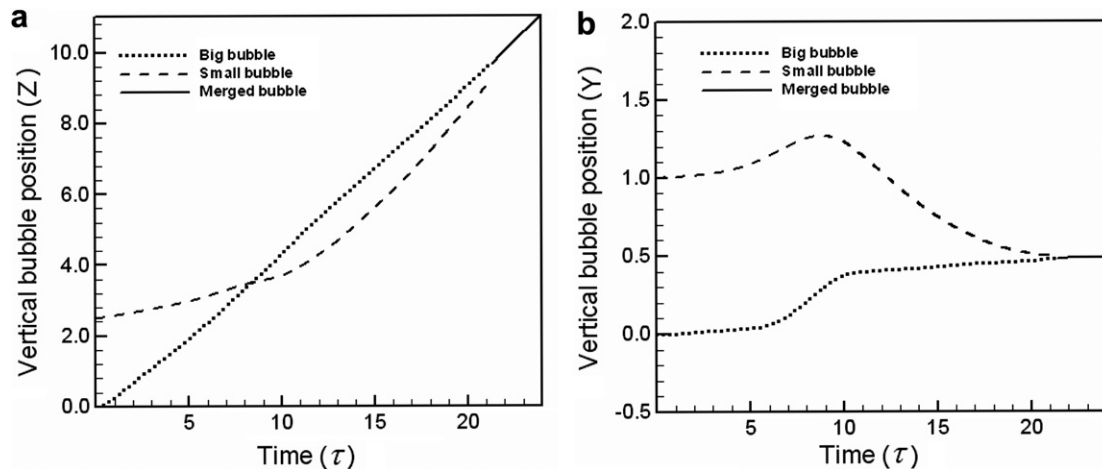
Fig. 19. Simulation predicted (a) vertical and (b) lateral movement in *Y*-direction of two rising bubbles and the merged bubble under the same conditions as those in Fig. 18.

4. Conclusion

The numerical algorithm used in this paper is a further extension of the algorithm given in [17] for simulating 3D gas bubbles rising in viscous liquids at high Reynolds and Bond numbers for the multiphase systems with large density and viscosity ratios such as air/water. To achieve this, mesh adaptation is implemented for both the front mesh and the background mesh, and a moving reference frame attached to the rising bubble is used to solve the governing incompressible Navier–Stokes equations. The solution method is a finite volume scheme based on the Semi-Implicit Method for Pressure-Linked Equations (SIMPLE), and the solver appears to be robust even in the range of high Reynolds numbers and high density/viscosity ratios. The bubble surface is tracked explicitly using an adaptive, unstructured triangular mesh. The model is integrated with the software package PARAMESH, a block-based adaptive mesh refinement (AMR) tool developed for parallel computing. It includes features such as background mesh adaptation and parallel implementation of solvers for the governing equations on supercomputers. The interpolations between the front mesh and the background mesh are done with the traditional Peskin approximation of the delta function. The current model has been applied to simulate a number of examples of 3D gas bubbles rising in viscous liquids, including air bubbles rising in water. The simulation results are compared with experimental observations in aspect of both the terminal bubble shape and the terminal bubble velocity. In addition, we use this model to predict the interaction between two bubbles rising in liquid. The numerical results illustrate the capability and feasibility of the current simulation method and provide us with some physical insights into the complex behavior of bubbles rising in viscous liquids.

References

[1] D. Bhaga, M.E. Weber, Bubbles in viscous liquids: shapes, wakes and velocities, J. Fluid Mech. 105 (1981) 1.
[2] T. Bonometti, J. Magnaudet, Transition from spherical cap to toroidal bubbles, Phys. Fluids 18 (2006) 052102.
[3] L.A. Bozzi, J.Q. Feng, T.C. Scott, A.J. Pearlstein, Steady axisymmetric motion of deformable drops falling or rising through a homoviscous fluid in a tube at intermediate Reynolds number, J. Fluid Mech. 336 (1997) 1.
[4] J.U. Brackbill, D.B. Kothe, C. Zenmach, A continuum method for modeling surface tension, J. Comput. Phys. 100 (1992) 335.
[5] B. Bunner, G. Tryggvason, Dynamics of homogenous bubbly flows. Part I: rise velocity and microstructure of the bubbles, J. Fluid Mech. 466 (2002) 17.
[6] L. Chen, S.V. Garimella, J.A. Reizes, E. Leonardi, The development of a bubble rising in a viscous liquid, J. Fluid Mech. 387 (1999) 61.
[7] R. Clift, J.R. Grace, M.E. Weber, Bubbles, Drops, and Particles, Academic Press, San Diego, 1978.
[8] R.M. Davies, F.I. Taylor, The mechanism of large bubbles rising through extended liquids and through liquids in tubes, Proc. Roy. Soc. London, Ser. A 200 (1950) 375.

[9] W. Dijkhuizen, E.I.V. van den Hengel, N.G. Deen, M. van Sint Annaland, J.A.M. Kuipers, Numerical investigation of closures for interface forces acting on single air-bubbles in water using volume of fluid and front tracking method models, Chem. Eng. Sci. 60 (2005) 6169.

[10] A.L. Fogelson, C.S. Peskin, A fast numerical method for solving the three-dimensional Stokes equations in the presence of suspended particles, J. Comput. Phys. 79 (1988) 50.

[11] J. Glimm, O. McBryan, R. Menikoff, D.H. Sharp, Front tracking applied to Rayleigh–Taylor instability, SIAM J. Sci. Stat. Comput. 7 (1986) 230.

[12] J. Glimm, J.W. Grove, B. Lindquist, O. McBryan, G. Tryggvason, The bifurcation of tracked scalar waves, SIAM J. Sci. Stat. Comput. 9 (1988) 61.

[13] J. Glimm, J.W. Grove, X.L. Li, D.C. Tan, Robust computational algorithms for dynamic interface tracking in three dimensions, SIAM J. Sci. Comput. 21 (2000) 2240.

[14] C.W. Hirt, B.D. Nichols, The volume of fluid (VOF) method for the dynamics of free boundaries, J. Comput. Phys. 39 (1981) 201.

[15] T.Y. Hou, J.S. Lowengrub, M.J. Shelley, Boundary integral methods for multicomponent fluids and multiphase materials, J. Comput. Phys. 169 (2001) 302.

[16] H.H. Hu, N.A. Patankar, M.Y. Zhu, Direct numerical simulation of fluid–solid system using the arbitrary Lagrangian–Eularian technique, J. Comput. Phys. 169 (2001) 427.

[17] J. Hua, J. Lou, Numerical simulation of bubble rising in viscous liquid, J. Comput. Phys. 222 (2007) 759.

[18] M. Ida, An improved unified solver for compressible and incompressible fluids involving free surfaces. Part I. Convection, Comput. Phys. Commun. 132 (2000) 44.

[19] D. Jacqmin, Calculation of two-phase Navier–Stokes flows using phase-field modeling, J. Comput. Phys. 155 (1999) 96.

[20] I.S. Kang, L.G. Leal, Numerical solution of axisymmetric, unsteady free-boundary problem at finite Reynolds number. I. Finite difference scheme and its application to the deformation of a bubble in a uniaxial straining flow, Phys. Fluids 30 (1987) 1929.

[21] M. Koebe, D. Bothe, J. Pruess, H.-J. Warnecke, 3D direct numerical simulation of air bubbles in water at high Reynolds number, in: Proceedings of the 2002 ASME Fluids Engineering Division Summer Meeting (FEDSM2002-31143), Montreal, Quebec, Canada, July 14–18, 2002.

[22] A. Koynov, J.G. Khinast, G. Tryggvason, Mass transfer and chemical reactions in bubble swarms with dynamics interface, AIChE J. 51 (2005) 2786.

[23] R. Krishna, M.I. Urseanu, J.M. van Baten, J. Ellenberger, Wall effects on the rise of single gas bubbles in liquids, Int. Commun. Heat Mass Transfer 26 (1999) 781.

[24] P. MacNeice, K.M. Olson, C. Mobarry, R. deFainchtein, C. Packer, PARAMESH: a parallel adaptive mesh refinement community toolkit, Comput. Phys. Commun. 126 (2000) 330.

[25] D.W. Moore, The rise of a gas bubble in viscous liquid, J. Fluid Mech. 6 (1959) 113.

[26] G. Mougin, J. Magnaudet, Wake-induced forces and torques on a zigzagging/spiraling bubble, J. Fluid Mech. 567 (2006) 185.

[27] M. Ohta, T. Imura, Y. Yoshida, M. Sussman, A computational study of the effect of initial bubble conditions on the motion of a gas bubble rising in viscous liquids, Int. J. Multiphase Flow 31 (2005) 223.

[28] S.J. Osher, J.A. Sethian, Fronts propagating with curvature dependent speed. Algorithms based on Hamilton–Jacobi formulations, J. Comput. Phys. 79 (1988) 12.

[29] S. Osher, R.P. Fedkiw, Level set methods: an overview and some recent results, J. Comput. Phys. 169 (2001) 463.

[30] S.V. Patankar, Numerical Heat Transfer and Fluid Flow, Hemisphere, New York, 1980.

[31] C.S. Peskin, Numerical analysis of blood flow in the heart, J. Comput. Phys. 25 (1977) 220.

[32] C.S. Peskin, B.F. Printz, Improved volume conservation in the computation of flows with immersed boundaries, J. Comput. Phys. 105 (1993) 33.

[33] C. Pozrikidis, Interfacial dynamics for Stokes flow, J. Comput. Phys. 169 (2001) 250.

[34] A. Prosperetti, Bubbles, Phys. Fluids 16 (2004) 1852.

[35] S. Quan, D.P. Schmidt, A moving mesh interface tracking method for 3D incompressible two-phase flows, J. Comput. Phys. 221 (2006) 761.

[36] H. Rusche, Computational fluid dynamics of dispersed two-phase flows at high phase fractions, Ph.D. Thesis, Imperial College of Science, Technology and Medicine, 2002.

[37] G. Ryskin, L.G. Leal, Numerical simulation of free-boundary problems in fluid mechanics. Part 2. Buoyancy-driven motion of a gas bubble through a quiescent liquid, J. Fluid Mech. 148 (1984) 19.

[38] A.S. Sangani, Sedimentation in ordered emulsions of drops at low Reynolds numbers, ZAMP 38 (1987) 542.

[39] R. Scardovelli, S. Zaleski, Direct numerical simulation of free-surface and interfacial flow, Annu. Rev. Fluid Mech. 31 (1999) 567.

[40] W.L. Shew, J.-F. Pinton, Viscoelastic effects on the dynamics of a rising bubble, J. Stat. Mech. (2006) P01009.

[41] S. Shin, D. Juric, Modelling three-dimensional multiphase flow using a level contour reconstruction method for front track with connectivity, J. Comput. Phys. 180 (2002) 427.

[42] M. van Sint Annaland, N.G. Deen, J.A.M. Kuipers, Numerical simulation of gas bubbles behaviour using a three-dimensional volume of fluid method, Chem. Eng. Sci. 60 (2005) 2999.

[43] M. van Sint Annaland, W. Dijkhuizen, N.G. Deen, J.A.M. Kuipers, Numerical simulation of behaviour of gas bubbles using a 3D front-tracking method, AIChE J. 52 (2006) 99.

[44] M. Sussman, P. Smereka, S. Osher, A level set approach for computing solutions to incompressible two-phase flows, J. Comput. Phys. 114 (1994) 146.

[45] T.D. Taylor, A. Acrivos, On the deformation and drag of a falling viscous drop at low Reynolds number, J. Fluid Mech. 18 (1964) 466.

[46] A. Tomiyama, G.P. Celata, S. Hosokawa, S. Yoshida, Terminal velocity of single bubbles in surface tension force dominant regime, Int. J. Multiphase Flow 28 (2002) 1497.

[47] G. Tryggvason, B.B. Bunner, A. Esmaeeli, D. Juric, N. Al-Rawahi, W. Tauber, J. Han, S. Nas, Y.J. Jan, A front-tracking method for the computations of multiphase flow, J. Comput. Phys. 169 (2001) 708.

[48] S.O. Unverdi, G. Tryggvason, A front-tracking method for viscous, incompressible, multi-fluid flows, J. Comput. Phys. 100 (1992) 25.

[49] M.M. Wu, M. Gharib, Experimental studies on the shape and path of small air bubbles rising in clean water, Phys. Fluids 14 (2002) 49.

[50] B. Yang, A. Prosperetti, S. Takagi, The transient rise of a bubble subject to shape or volume changes, Phys. Fluids 15 (2003) 2640.